J. Fluid Mech. (2020), *vol.* 897, A26. © The Author(s), 2020.
Published by Cambridge University Press
doi:10.1017/jfm.2020.347

Feedback control of vortex shedding using a resolvent-based modelling approach

Bo Jin[1,†], **Simon J. Illingworth**[1] **and Richard D. Sandberg**[1]

[1]Department of Mechanical Engineering, University of Melbourne, VIC 3010, Australia

(Received 2 September 2019; revised 16 April 2020; accepted 29 April 2020)

An investigation of optimal feedback controllers' performance and robustness is carried out for vortex shedding behind a two-dimensional cylinder at low Reynolds numbers. To facilitate controller design, we present an efficient modelling approach in which we utilise the resolvent operator to recast the linearised Navier–Stokes equations into an input–output form from which frequency responses can be computed. The difficulty of applying modern control design techniques to high-dimensional flow systems is overcome by using low-order models identified from frequency responses. These low-order models are used to design optimal controllers using $\mathcal{H}_\infty$ loop shaping. Two distinct single-input single-output control arrangements are considered. In the first arrangement, a velocity sensor located in the wake drives a pair of body forces near the cylinder. Complete suppression of shedding is observed up to $Re = 110$. Due to the convective nature of vortex shedding and the corresponding time delays, we observe a fundamental trade-off: the sensor should be close enough to the cylinder to avoid excessive time lag, but it should be kept sufficiently far from the cylinder to measure unstable modes developing downstream. These two conflicting requirements become more difficult to satisfy for larger Reynolds numbers. In the second arrangement, we consider a practical set-up with an actuator that oscillates the cylinder according to the lift measurement. The system is stabilised up to $Re = 100$, and we demonstrate why the performance of the resulting feedback controllers deteriorates more rapidly with increasing Reynolds number. The challenges of designing robust controllers for each control set-up are also analysed and discussed.

Key words: vortex shedding, vortex instability

1. Introduction

In the last few decades, the control of fluid dynamics has received considerable attention from researchers and engineers. Indeed, the ability to manipulate fluid flows can be of tremendous benefit in a number of applications. A typical example is the flow past a circular cylinder which becomes unstable above a critical Reynolds number near 47 and results in vortex shedding (Jackson 1987; Provansal, Mathis & Boyer 1987; Zebib 1987; Dušek, Le Gal & Fraunié 1994). This gives rise to strong force fluctuations which are responsible for structural vibrations, acoustic noise and

† Email address for correspondence: bjin1@student.unimelb.edu.au

resonance (Williamson 1996). Much research has been conducted on the suppression of vortex shedding using either passive strategies (without additional energy input) or active strategies (with an external energy source), as summarised by Choi, Jeon & Kim (2008).

1.1. *Feedback control and model reduction*

Closed-loop control, where actuators operate actively according to real-time measurements of the flow field, is a robust and energetically efficient way to control fluid flows. In some studies, feedback control has been applied without knowledge of the flow dynamics. Simple proportional feedback laws were designed by trial and error to eliminate vortex shedding in various control arrangements, such as loudspeakers (Roussopoulos 1993), blowing/suction slots (Park, Ladd & Hendricks 1994; Gunzburger & Lee 1996) and small rotary control cylinders (Muddada & Patnaik 2010). Zhang, Cheng & Zhou (2004) developed a proportional–integral–derivative controller to suppress vortex-induced vibration on a spring-supported cylinder. A further investigation of proportional, proportional–derivative, proportional–integral and proportional–integral–derivative feedback control was carried out (see Son, Jeon & Choi 2011; Son & Choi 2018) to compare and optimise control laws for suppression of vortex shedding. The parameters in these control laws were chosen based on either a brute-force approach or physical intuition.

Although these studies have met with some success, they are not model-based. There exists a large set of well-developed and powerful control design tools providing efficient and robust methods for model-based control design. However, due to the nonlinearity and high dimensionality of the Navier–Stokes equations, they are in general computationally intractable to apply directly to fluid flows. This difficulty can be bypassed by means of flow linearisation (Kim & Bewley 2007; Sipp *et al.* 2010) and model reduction (Rowley & Dawson 2017; Taira *et al.* 2017), where important features of fluid flows are approximated by low-order linear models.

A number of techniques have been developed to approximate flow dynamics by reduced-order models (ROMs) for the purpose of control design, such as proper orthogonal decomposition (POD), balanced POD, Eigensystem Realisation Algorithm (ERA), etc. One of the earliest studies is that of Aubry *et al.* (1988), who approximated important features of the boundary layer by a low-dimensional nonlinear model based on POD. The method has shown its effectiveness in later research for flow control problems, such as cylinder wake (Gillies 1998; Singh *et al.* 2001) and channel flow (Ilak & Rowley 2008).

Much recent work on flow control has focused on linear input–output formulations of flow systems (Bagheri *et al.* 2009). Using this approach, the governing equations are projected onto the most controllable and observable modes to capture important input–output dynamics. These modes can be generated by either balanced POD (Rowley 2005) or the ERA (Juang & Pappa 1985). These methods were originally designed for stable systems of large dimension and were subsequently extended to unstable systems either by a state-projection method (Ahuja & Rowley 2010) or by limiting the simulation time (Flinois & Morgans 2016). A detailed comparison between these methods was presented by Ma, Ahuja & Rowley (2011) using the example of the flow past an inclined flat plate. Without using any adjoint information, the ERA produced the same ROMs as those given by balanced POD, which allows its direct application to flow systems using only simulation or experimental data (Belson *et al.* 2013; Illingworth 2016; Yao & Jaiman 2017*a*,*b*). A stochastic modelling

approach was also presented for three-dimensional bluff body wakes and the model was used in the design of a feedback controller which reduced the drag on a bluff body (Brackston *et al.* 2016; Brackston, Wynn & Morrison 2018).

The accuracy of these snapshot-based truncation methods is generally dependent on the time interval chosen and the final time of simulation or experimental data. Recently, model reduction based on resolvent analysis has shown good potential. The method has been applied to efficiently identify physical flow structures in a broad range of nonlinear flows, such as cavity flow (Gómez *et al.* 2016), flat-plate boundary layer flow (Sipp & Marquet 2013), pipe flow (McKeon & Sharma 2010) and flow past a cylinder (Symon *et al.* 2018). The method allows direct formulation of the flow system in the frequency domain. There is no special treatment required for unstable systems and no restriction on the frequency range over which the linear dynamics can be captured.

Some recent studies have demonstrated a significant influence of actuator–sensor choice and placement on the performance and robustness of feedback controllers. In a two-dimensional Blasius boundary layer, the type and relative position of the sensor and the actuator have been shown to be crucial to the controller's performance (Belson *et al.* 2013). Some early works indicated that any sensors should be placed based on the unstable global modes, and that any actuators should be placed based on the corresponding adjoint modes (Åkervik *et al.* 2007; Bagheri *et al.* 2009). Previous work conducted by Giannetti & Luchini (2007) introduced a region that describes the overlap between eigenmodes and adjoint eigenmodes known as the wavemaker region. Placing both the actuator and sensor in this region of the flow resulted in closed-loop control performance that was almost optimal (Chen & Rowley 2011). However, the wavemaker region does not represent the optimal location for actuators or sensors for the Ginzburg–Landau system (Chen & Rowley 2011; Oehler & Illingworth 2018). Indeed Oehler & Illingworth (2018) found that the wavemaker region has no special significance for the placement of actuators and sensors. They investigated optimal actuator–sensor placement for the one-dimensional complex Ginzburg–Landau system and found that, with increasing instability, the optimal actuator or sensor location moves further away from that predicted by the wavemaker region.

1.2. *This article*

The current work uses an efficient modelling approach with an input–output formulation based on resolvent analysis (Sipp & Marquet 2013). This allows one to directly obtain frequency responses for a broad range of control configurations. The MATLAB package VECTFIT (Gustavsen 2013) is used to fit ROMs to these frequency responses. The $\mathcal{H}_\infty$ loop shaping method (Glover & McFarlane 1989) is employed to design optimal feedback controllers and also provides a stability margin which serves as an indicator of the control performance achieved. We demonstrate the effectiveness of the method for the feedback control of the instabilities that lead to vortex shedding for the flow past a two-dimensional circular cylinder.

Another contribution of this work is to analyse the effect of different control configurations on control performance and robustness. We shall see that in-flow actuator and sensor outperforms the body-mounted set-up. A further investigation of optimal in-flow sensor placement in a two-dimensional flow allows us to observe a fundamental trade-off which is consistent with the conclusions of Belson *et al.* (2013) and Oehler & Illingworth (2018). We show that the deterioration of the control performance in a bluff body flow also has a variety of root causes

(Hoagg & Bernstein 2007). By examining different sensor positions for a range of Reynolds numbers, we demonstrate how these roots affect the performance of controllers as well as possible physical mechanisms behind them.

The article starts with the definition of the flow and control configurations in § 2. In § 3, we form ROMs using an input–output framework and explain the numerical set-ups and control design techniques. The results and analysis of the in-flow and body-mounted control set-ups are presented in §§ 4 and 5, respectively. Conclusions are given in § 6.

2. Problem formulation

The objective of feedback control is to completely suppress vortex shedding behind a two-dimensional circular cylinder. In other words, we attempt to drive the flow towards its unstable steady state (base flow), around which the Navier–Stokes equations are linearised. The governing equations are the incompressible Navier–Stokes equations with external forcing:

$$\frac{\partial \boldsymbol{u}}{\partial t} + \boldsymbol{u}\cdot\nabla\boldsymbol{u} = -\nabla p + \nu\nabla^2\boldsymbol{u} + \boldsymbol{f}', \quad \nabla\cdot\boldsymbol{u} = 0, \tag{2.1a,b}$$

where the source term $\boldsymbol{f}' = [f_x' \;\; f_y']^{\mathrm{T}}$ in the momentum equation models the external forcing which is assumed to have zero mean. To investigate the instability of the cylinder flow near its steady state, we perform an input–output analysis by linearising about the laminar base flow $(\boldsymbol{U}, P)$:

$$\frac{\partial \boldsymbol{u}'}{\partial t} + \boldsymbol{U}\cdot\nabla\boldsymbol{u}' + \boldsymbol{u}'\cdot\nabla\boldsymbol{U} = -\nabla p' + \nu\nabla^2\boldsymbol{u}' + \boldsymbol{f}', \quad \nabla\cdot\boldsymbol{u}' = 0. \tag{2.2a,b}$$

Here, $(\boldsymbol{u}', \; p')$ represents the unsteady components of velocity and pressure which are assumed to be small perturbations about the steady state and ν is the kinematic viscosity. The Reynolds number is defined as $Re = U_\infty D/\nu$, where U_∞ is the free-stream velocity and D is the diameter of the cylinder. The range of Reynolds numbers considered is $Re \in [50, 110]$ and all lengths are non-dimensionalised by D. At these Reynolds numbers the cylinder wake has a single linearly unstable mode which drives the flow to periodic self-sustained limit-cycle oscillations (vortex shedding). The controllers we design aim to keep perturbations small, and so the nonlinear term $\boldsymbol{u}'\cdot\nabla\boldsymbol{u}'$ can be neglected. This formulation allows us to use existing linear control theory and analysis techniques.

In-flow and body-mounted sensors and actuators are used and compared. We choose two simple set-ups as representatives of in-flow and body-mounted control arrangements and figure 1 shows a schematic of them.

2.1. *In-flow control set-up*

In the first control set-up, the momentum equation (2.2) is forced by a pair of antisymmetric body forces $\boldsymbol{f}'$ that serve as an in-flow actuator:

$$\boldsymbol{f}' = \boldsymbol{B}(x, y)[u(t) + w(t)], \tag{2.3}$$

where $u(t)$ is the actuator signal provided by a transverse velocity sensor positioned a distance d downstream of the cylinder, $w(t)$ is a disturbance from the actuator and $\boldsymbol{B}(x, y)$ is the spatial distribution of the actuator and disturbance. More specifically,

$$\boldsymbol{B} = \begin{bmatrix} \cos\theta(\mathcal{S}(A, \sigma, r, \theta) - \mathcal{S}(A, \sigma, r, -\theta)) \\ \sin\theta(\mathcal{S}(A, \sigma, r, \theta) + \mathcal{S}(A, \sigma, r, -\theta)), \end{bmatrix}, \tag{2.4}$$

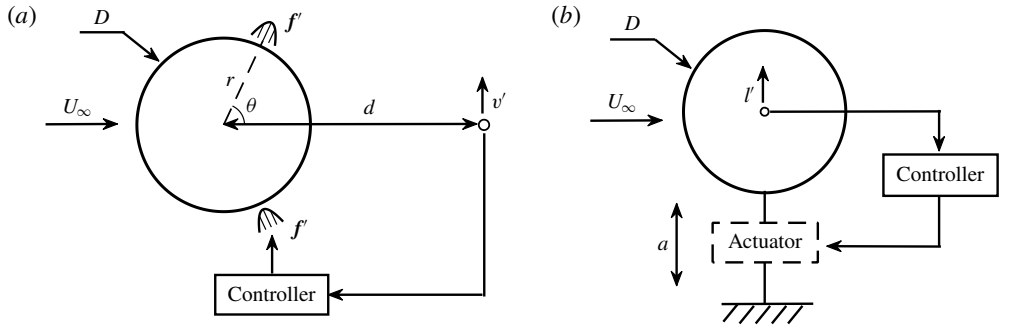

FIGURE 1. (*a*) A pair of body forces $\boldsymbol{f}'$ applied near the cylinder surface cooperates with a velocity sensor placed on the centreline at a distance d from the centre of the cylinder. (*b*) The force sensor is placed on the cylinder to measure the lift l' which is fed to the actuator that controls the transverse acceleration a of the cylinder.

where

$$\mathcal{S}(A, \sigma, r, \theta) = \frac{A}{2\pi\sigma^2} \exp\left(-\frac{(x - r\cos\theta)^2 + (y - r\sin\theta)^2}{2\sigma^2}\right), \tag{2.5}$$

where the magnitude is $A = 1.0$ and the standard deviation $\sigma = 0.1$. The centres of the above distributions are near the separation points at a distance of $r = 0.6$ from the cylinder's centre and an angle of $\theta = \pm 70^\circ$ from the cylinder's downstream-pointing horizontal. We fix the form and the location of the actuator and vary only the sensor position along the centreline to investigate the influence of sensor placement. This arrangement is similar to that used by Illingworth (2016).

2.2. *Body-mounted control set-up*

The second control set-up considered uses a body-mounted actuator and a body-mounted sensor. Similar to a fluid–structure interaction system, we consider an oscillatory cylinder whose transverse acceleration a is controlled according to the feedback signal provided by a lift sensor attached on the cylinder. Optimal feedback controllers are designed for different Reynolds numbers to suppress vortex shedding and the vibration of the bluff body.

3. Modelling and control methods

3.1. *State-space formulation and system identification*

The linearised Navier–Stokes equations can be written in standard state-space form which is useful for performing input–output analysis. To evaluate the linear dynamics of a flow system, it is convenient to take Laplace transforms. Introducing the transformation into (2.2), we obtain the equations

$$s\hat{\boldsymbol{u}} + \boldsymbol{U}\cdot\nabla\hat{\boldsymbol{u}} + \hat{\boldsymbol{u}}\cdot\nabla\boldsymbol{U} = -\nabla\hat{p} + \nu\nabla^2\hat{\boldsymbol{u}} + \hat{\boldsymbol{f}}, \quad \nabla\cdot\hat{\boldsymbol{u}} = 0, \tag{3.1a,b}$$

where $(\hat{\boldsymbol{u}},\ \hat{p})$ and $\hat{\boldsymbol{f}}$ represent the (complex-valued) spatial structure of the velocity and body forcing and $s = \sigma + j\omega$ is the Laplace variable. Thus, the transfer function

between the external forcing and response can be written as

$$\begin{bmatrix}\hat{\boldsymbol{u}}\\ \hat{p}\end{bmatrix} = (s\mathcal{E}-\mathcal{A})^{-1}\begin{bmatrix}\hat{\boldsymbol{f}}\\ 0\end{bmatrix}, \tag{3.2}$$

where $(s\mathcal{E}-\mathcal{A})^{-1}$ is known as the resolvent operator and $\mathcal{A}$ is the linearised Navier–Stokes operator around the base flow:

$$\mathcal{A}=\begin{bmatrix}-\boldsymbol{U}\cdot\boldsymbol{\nabla}-()\cdot\boldsymbol{\nabla}\boldsymbol{U}+\nu\nabla^2 & -\boldsymbol{\nabla}\\ \boldsymbol{\nabla}\cdot() & 0\end{bmatrix}, \quad \mathcal{E}=\begin{bmatrix}I & 0\\ 0 & 0\end{bmatrix}. \tag{3.3a,b}$$

We now consider writing (3.2) in state-space form for a linear, time-variant dynamical system $P(s)$:

$$\begin{aligned} s\mathcal{E}\boldsymbol{x} &= \mathcal{A}\boldsymbol{x}+\mathcal{B}e,\\ y &= \mathcal{C}\boldsymbol{x}+\mathcal{D}e,\end{aligned} \tag{3.4}$$

where $\boldsymbol{x}=[\hat{\boldsymbol{u}}\quad \hat{p}]^{\mathrm{T}}$ is the system state, e is an input vector of dimension p and y is an output vector of dimension q. The feedback control arrangement used here is single-input single-output with $p=q=1$. The vector $\mathcal{B}$ is determined by the shape of the actuation, which is from the spatial discretisation of the external forcing term $\hat{\boldsymbol{f}}$. The matrices $\mathcal{C}$ and $\mathcal{D}$ represent output and feed-forward dynamics, respectively. The transfer function between the output y and input e can then be written as

$$P(s)=\mathcal{C}(s\mathcal{E}-\mathcal{A})^{-1}\mathcal{B}+\mathcal{D}. \tag{3.5}$$

In general, $P(s)$ is of high dimension, which makes the control design problem computationally intractable. However, it is feasible to solve this linear system and get the frequency response data from the actuation to the measurement. Reduced-order models can then be formed for the corresponding frequency responses using the vector-fitting algorithm VECTFIT (Gustavsen & Semlyen 1999; Gustavsen 2006; Deschrijver *et al.* 2008). VECTFIT identifies a ROM $\widetilde{P}(s)$ of a significantly smaller dimension N in the rational form

$$\widetilde{P}(s)=\sum_{m=1}^{N}\frac{r_m}{s-a_m}+sh+d, \tag{3.6}$$

where the poles a_m, residues r_m and terms d and h are identified such that the frequency response of $\widetilde{P}(s)$ is within a distance ϵ of the original system $P(s)$ over a broad frequency range.

3.2. *Feedback controller design*

The feedback controller is designed based on the ROM $\widetilde{P}(s)$ using $\mathcal{H}_\infty$ loop shaping. The control block diagram is shown in figure 2, where $\hat{w}$ represents disturbances from the actuator and n represents noise at the sensor. We assume a positive feedback configuration as illustrated in figure 2. The controller $K(s)$ for plant $P(s)$ is designed using the loop-shaping design method of Glover & McFarlane (1989) which maximises the normalised coprime stability margin $b(\widetilde{P}, K)$ of the plant–controller feedback loop

$$b=\left\|\begin{bmatrix}K\\ I\end{bmatrix}(I+\widetilde{P}K)^{-1}\begin{bmatrix}\widetilde{P} & I\end{bmatrix}\right\|_\infty^{-1}, \tag{3.7}$$

where $b\in[0,1]$, which can be maximised over all stabilising K to give

$$b_{opt}(\widetilde{P})=\sup_K b(\widetilde{P},K). \tag{3.8}$$

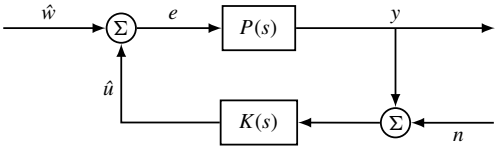

FIGURE 2. Block diagram of the closed-loop control system.

Physically, b_{opt} is an indication of the robustness of the closed-loop system to unmodelled dynamics and also serves as a performance measure: the larger the value of b_{opt}, the better the performance and the greater the robustness of the closed-loop system.

For single-input single-output systems as considered here, a compensator which weights the plant according to the control objectives is used of the form

$$W(s) = k\frac{a^2}{(s+a)^2}. \tag{3.9}$$

The parameters k and a are chosen such that the gain of the weighted plant is sufficiently high at frequencies where good disturbance attenuation is required and is sufficiently low at high frequencies where modelling uncertainties will be greatest (Illingworth 2016).

3.3. *Numerical set-up*

We consider an incompressible flow with free-stream velocity U_∞ past a two-dimensional circular cylinder of diameter D. Simulations are conducted on the computing platform FEniCS (Logg, Mardal & Wells 2012) which has been extensively used for fluid mechanics (Mortensen, Langtangen & Wells 2011; Nguyen *et al.* 2019; Vasilyeva *et al.* 2019). Three versions of the flow are solved: the steady solution of (2.1) (base flow), the linearised perturbation equation (3.4) in state-space form and the fully nonlinear Navier–Stokes equations. We employ the same computational domain as that used by Leontini *et al.* (2006), as shown in figure 3, and discretise using Taylor–Hood finite elements over a structured mesh. In order to appropriately resolve the details of the flow, the mesh points are clustered smoothly near the cylinder and in the wake. More specifically, the mesh consists of 5.46×10^4 triangles and the minimum wall-normal size around the cylinder is 0.01. A backward Euler scheme is used for time discretisation ($\Delta t = 0.01$) in the direct numerical simulations with the maximum Courant number below 0.6 to ensure accuracy.

The base flow $(\boldsymbol{U}, P)$, which is governed by the unforced steady Navier–Stokes equations, is solved using a Newton method. The corresponding boundary conditions are summarised in figure 3. Dirichlet boundary conditions are imposed at the inlet Γ_{in} $(x < 0)$ and at the cylinder surface Γ_{wall} (centred at $x = y = 0$):

$$U = 1, \quad V = 0 \quad \text{on } \Gamma_{in}, \tag{3.10a,b}$$

$$U = 0, \quad V = 0 \quad \text{on } \Gamma_{wall}. \tag{3.10c,d}$$

Symmetry conditions are enforced on the top and bottom boundaries Γ_{top} and Γ_{bottom} $(0 < x/D < 23, y/D = \pm 15)$:

$$\frac{\partial U}{\partial y} = 0, \quad V = 0 \quad \text{on } \Gamma_{top} \cup \Gamma_{bottom}, \tag{3.11a,b}$$

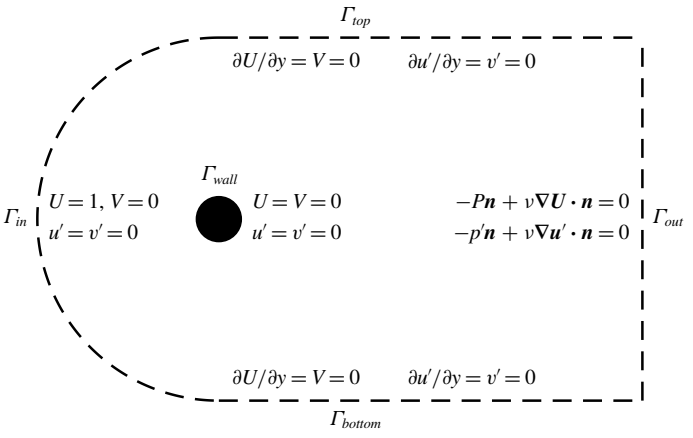

FIGURE 3. Computational domain and boundary conditions for the steady and unsteady linearised Navier–Stokes equations for the in-flow set-up.

while the pressure and the velocity are combined into the standard outflow conditions on the outlet boundary Γ_{out} ($x/D = 23$, $-15 < y/D < 15$):

$$-P\boldsymbol{n} + \nu\nabla\boldsymbol{U}\cdot\boldsymbol{n} = 0 \quad \text{on } \Gamma_{out}, \tag{3.12}$$

where $\boldsymbol{n}$ denotes the outward-pointing normal vector on the boundary. The base flow is the same for all control set-ups. Vorticity contours for the base flow are shown in figure 4(*a*) at $Re = 60$, 80 and 100.

The basic boundary conditions for the perturbation ($\boldsymbol{u}'$, p') are also depicted in figure 3. For the in-flow control set-up, the linear perturbation system has the same boundary conditions as the base flow except at the inlet where homogeneous boundary conditions ($u' = v' = 0$) are enforced to ensure zero perturbations at infinity. In the body-mounted control set-up, the flow is solved in an accelerated frame of reference attached to the cylinder instead of moving the cylinder directly. For this, the transverse acceleration of the frame a is treated as an extra forcing term $\boldsymbol{f}' = [0 \quad a]^{\mathrm{T}}$. Thus, the boundary conditions at the inlet, top and bottom boundaries are modified (Leontini *et al.* 2006):

$$u' = 0, \quad v' = \int_0^t a(t)\,\mathrm{d}t \quad \text{on } \Gamma_{in}, \tag{3.13a,b}$$

$$\frac{\partial u'}{\partial y} = 0, \quad v' = \int_0^t a(t)\,\mathrm{d}t \quad \text{on } \Gamma_{top} \cup \Gamma_{bottom}, \tag{3.13c,d}$$

where zero initial conditions are assumed. In the linear state-space model (3.4), these boundary conditions are enforced in the frequency domain by applying Laplace transforms:

$$\hat{u} = 0, \quad \hat{v} = \frac{\hat{a}}{s} \quad \text{on } \Gamma_{in}, \tag{3.14a,b}$$

$$\frac{\partial \hat{u}}{\partial y} = 0, \quad \hat{v} = \frac{\hat{a}}{s} \quad \text{on } \Gamma_{top} \cup \Gamma_{bottom}. \tag{3.14c,d}$$

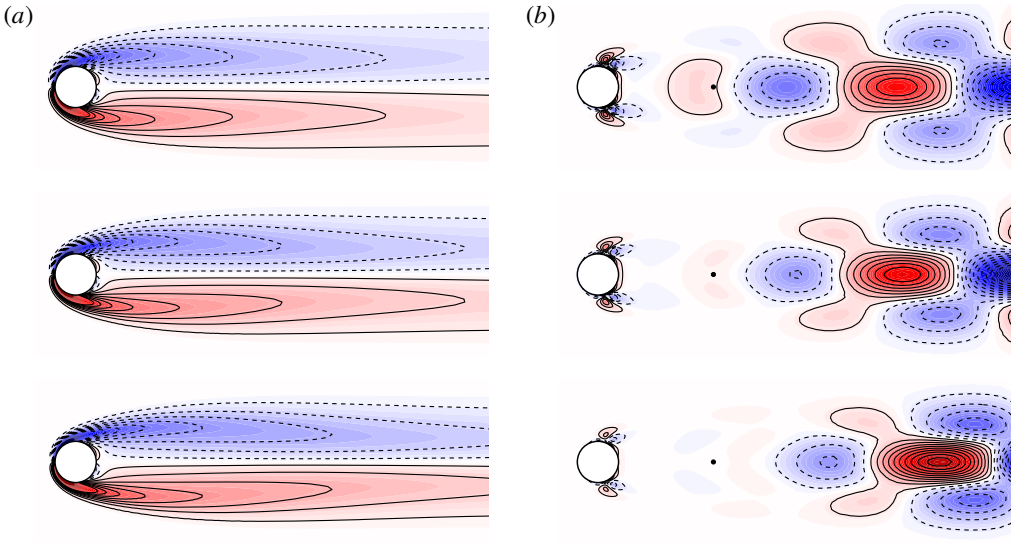

FIGURE 4. Vorticity contours (dashed lines for negative and solid lines for positive vorticity) for (*a*) the unstable base flow and (*b*) the perturbation system (normalised, real part) forced by the harmonic forcing at the unstable frequency for $Re = 60$, 80 and 100 (from top to bottom). A velocity sensor (•) is placed a distance d downstream of the cylinder. Contours in (*a*,*b*) share the same scale for comparison.

The stability analysis of the base flows and discretised perturbation systems have been validated using the results of Barkley (2006). To validate the controllers, direct numerical simulations are performed using the IPCS (Incremental Pressure Correction Scheme) method which has been extensively tested in Logg *et al.* (2012). The corresponding boundary conditions are modified based on the identity $(\boldsymbol{u}, p) = (\boldsymbol{U} + \boldsymbol{u}',\ \ P + p')$.

4. In-flow control set-up case

In the first instance, an in-flow control set-up is considered in which a single sensor is placed in the wake and a single actuator is applied near the cylinder (see figure 1*a*). We first form ROMs for model-based control, and the performance and robustness of all controllers are characterised and compared. We vary the Reynolds number and the location of the velocity sensor to investigate the influence of sensor placement on control at different Reynolds numbers.

4.1. *Open-loop system identification*

Figure 4(*b*) shows the normalised vorticity field of the corresponding perturbation system $P(s)$ actuated by the body force $\hat{\boldsymbol{f}}$ at the unstable frequency $s = j\omega_u$ (i.e. the resolvent operator between the input and output in (3.2)). The shear layer emanating from the separation point is disturbed by the actuator and grows into a large-scale vortical structure downstream. As the Reynolds number increases, the large vortical structure formed by the shear layer appears increasingly far downstream. This is because the length of the absolutely unstable region behind the circular cylinder increases with increasing Reynolds number. It is noteworthy that the absolutely

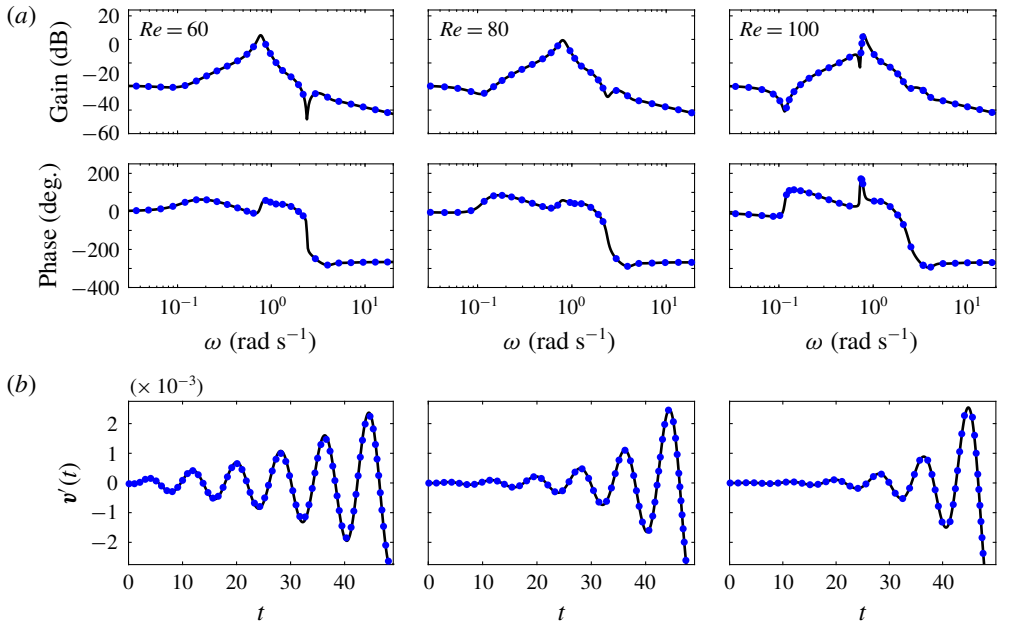

FIGURE 5. (*a*) Frequency responses from $P(j\omega)$ (——) compared to those from ROMs $\widetilde{P}(j\omega)$ (•, blue) at $Re = 60$, 80 and 100. (*b*) The corresponding open-loop impulse responses from numerical simulations. The results for $Re = 60$ and 80 are multiplied by 20 and 3, respectively, so that the same scale can be used.

unstable region has the opposite trend of length variation for the linear flow (base flow) when compared to the nonlinear (mean) flow (Pier 2002).

After obtaining the base flow, the transfer function between the actuator signal and the sensor measurement, denoted by $\widetilde{P}(s)$, is to be determined for control design. Instead of harvesting data from direct numerical simulations (e.g. Dahan, Morgans & Lardeau 2012; Illingworth 2016), we obtain frequency responses by solving (3.5) directly for harmonic inputs ($s = j\omega$) over a broad range of frequencies. The ROMs are identified from the gain and phase of the response data by utilising a vector-fitting algorithm (Gustavsen 2013). The frequency range chosen here is $\omega \in [10^{-6}, 10^{6}]$ rad s^{-1} with 250 sampling points spaced logarithmically. At each Reynolds number, the computational cost is less than five minutes using a direct LU solver (Amestoy *et al.* 2001, 2006) and a standard node on a cluster. Figure 5(*a*) shows comparisons of response data near the unstable frequency ($\omega \approx 0.8$ rad s^{-1}) between the linear perturbation systems $P(s)$ and the identified ROMs $\widetilde{P}(s)$ at $Re = 60$, 80 and 100 with the velocity sensor placed at $d = 2.8D$. The order (or dimension) of $\widetilde{P}(s)$ is chosen such that the fitting residual ϵ is below 10^{-5}. This is achieved with an order of 30 or less for all Reynolds numbers considered.

The accuracy of the ROMs is validated by the excellent agreement between the open-loop impulse responses from these models and direct numerical simulations, which is summarised in figure 5(*b*). Due to the small-perturbation assumption, the magnitude of the impulse equals 1×10^{-4} and the linearity of the flow systems is also confirmed. Thus, the ROMs found are good approximations of the true systems.

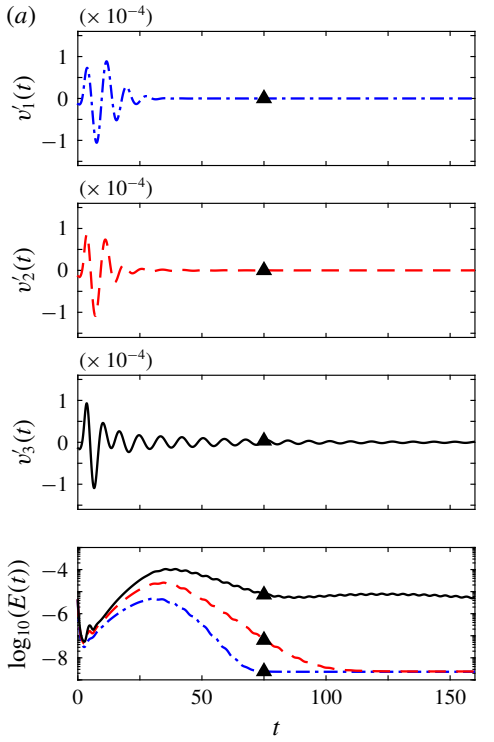

(c)

Re	*k*	*a*	b_{opt}	*d*
60	2.6	9.9	0.3952	2.8*D*
80	4.6	10.0	0.3005	2.8*D*
100	11.3	1.0	0.2495	2.8*D*

FIGURE 6. Direct numerical simulation results of closed-loop systems. (*a*) Time evolution of the transverse velocity at the sensor (•) and the total perturbation energy $E(t)$ in log scale at $Re = 60$ (– · –, blue), $Re = 80$ (- -, red) and $Re = 100$ (——). (*b*) Vorticity contours (dashed lines for negative and solid lines for positive vorticity) for the perturbation systems at $t = 75$ (▲) at $Re = 60$, 80 and 100 (from top to bottom). All contour plots share the same colour range. (*c*) Table of parameters.

4.2. *Model-based feedback control*

Based on the identified ROMs, we design an optimal feedback controller for each model and ensure that the controller satisfies closed-loop stability. The parameters in the compensator weight are determined after searching different value combinations to achieve the largest optimal stability margin b_{opt}. The controllers are implemented in the full nonlinear Navier–Stokes system with an impulse from the actuator of magnitude 10^{-3}. The resulting performance of the controllers for each of the cases described in § 4.1 is shown in figure 6.

The stabilising effect of the controller for each case is observed from the time evolution of the transverse velocity $(v_1'/v_2'/v_3')$ at the sensor, as shown in figure 6(*a*). More convincing evidence for the complete suppression of vortex shedding is the total perturbation energy plotted beneath, which is defined as

$$E(t) = \frac{1}{2}\int_{\Omega} (u'^2(x,\ y,\ t) + v'^2(x,\ y,\ t))\,\mathrm{d}x\,\mathrm{d}y, \tag{4.1}$$

where u' and v' are the streamwise and transverse perturbation velocity components, respectively. It is clear that the controller for $Re = 60$ performs best with the strongest

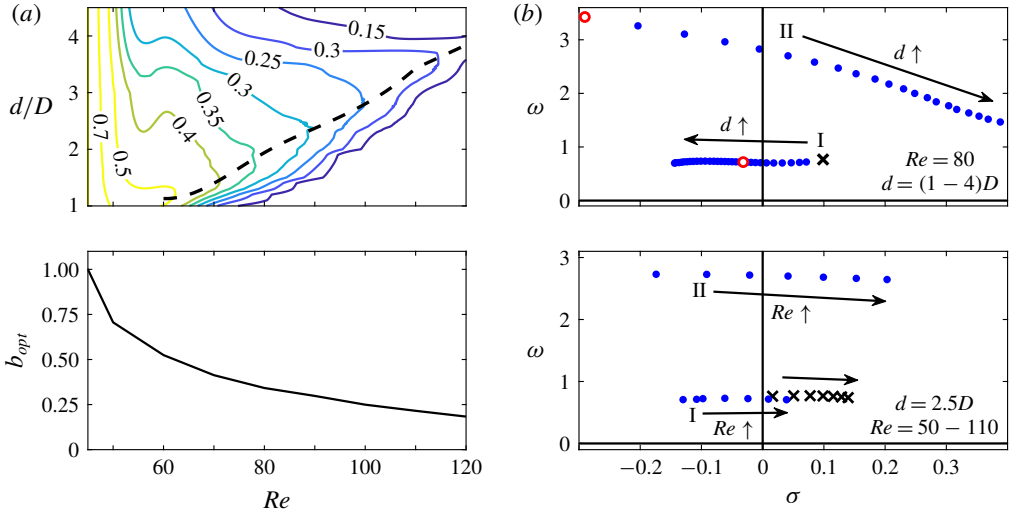

FIGURE 7. (*a*) Optimal sensor locations (the ridge - -) and contour plot of optimal stability margin b_{opt} against Reynolds number and sensor location d. And the largest b_{opt} (——) that can be achieved at different Reynolds numbers is plotted beneath. (*b*) Loci of unstable poles (×) and critical zeros (•, blue; ○, red) of transfer functions $\widetilde{P}(s)$ for two cases. Top: different sensor locations at $Re = 80$. Bottom: different Reynolds numbers with a sensor placed at $d = 2.5D$ downstream of the cylinder.

attenuation. Although the perturbation energy for $Re = 100$ remains large after $t = 150$, a decreasing trend is quite clear. Figure 6(*b*) shows the instantaneous vorticity perturbation fields for all three cases at $t = 75$. The perturbation vorticity at $Re = 60$ stays small without observable vortex shedding whereas at a higher Reynolds number of 80, the vorticity remains small near the sensor but is stronger downstream. At the highest Reynolds number of 100, the vorticity is far stronger with clear vortex shedding, which is consistent with the oscillations of v_3'. From the comparison between all three cases, we can see that perturbations are harder to control at higher Reynolds numbers.

The performance of each controller can be quantified using the optimal stability margin b_{opt}, which is summarised in figure 6(*c*) together with other important parameters. Based on the comparison of b_{opt} between the three cases, we can draw a conclusion consistent with the analysis above: the higher the Reynolds number, the smaller the optimal stability margin b_{opt} achieved by the optimal feedback controller.

4.3. *Optimal sensor placements*

The preliminary investigation summarised in figure 6 indicates a severe deterioration of control performance with increasing Reynolds number for a fixed velocity sensor. To draw more general conclusions about control performance, we vary the position of the velocity sensor along the centreline at different Reynolds numbers. For each case, the position and the form of the actuator are unchanged, and we identify a new ROM from response data at the corresponding Reynolds number. The performance of the $\mathcal{H}_\infty$-optimal controller for each case is quantified by the optimal stability margin b_{opt} and summarised as a function of Reynolds number and sensor location d in figure 7(*a*).

First, we focus on the optimal sensor location where the optimal controller shows the best performance at each Reynolds number. Generally, the ideal position for a sensor should allow not only the measurement of the instability developing downstream but also the timely feedback of information to the actuator. Figure 7(*a*) first shows a contour map of the optimal stability margin b_{opt} against Reynolds number and sensor location d. It is clear that a ridge exists which indicates the optimal sensor location as a function of Reynolds number. At each Reynolds number, the optimal controller for the sensor at the ridge line performs better than those for other sensor locations. However, the optimal stability margin b_{opt} on the ridge decreases sharply with increasing Reynolds number, which is shown in the panel beneath the contour map.

Therefore, a fundamental trade-off can be concluded from figure 7(*a*): the sensor should be close enough to the cylinder to reduce the time delay due to convection, but it should also be far enough from the cylinder to measure important information (e.g. unstable eigenmodes) developing downstream. The compromise between these two conflicting requirements becomes harder to satisfy with increasing Reynolds number, which leads to the optimal sensor location moving downstream linearly. Similar results have been observed in recent work (Oehler & Illingworth 2018) that considers feedback control of the linearised Ginzburg–Landau system.

Generally, the performance and robustness of an optimal controller, as quantified by the optimal stability margin b_{opt}, can be linked to the zeros and poles of the corresponding system. Mathematically, poles and zeros of a system are roots of the denominator and numerator of the corresponding transfer function, which determine whether the system is stable, and how the system performs. More specifically, poles capture the form of each component in the system response, whereas zeros reflect how these components combine together, including the phase and magnitude of each component generated by each pole. To investigate these roots in the perturbation system, we consider two cases: (i) fixing the Reynolds number at $Re = 80$ and moving the sensor from $d = 1D$ to $d = 4D$; (ii) fixing the sensor position at $d = 2.5D$ and increasing the Reynolds number from 50 to 110. The root loci of these two cases are computed, where unstable poles and two kinds of critical zeros (which we label I and II) are identified and plotted in figure 7(*b*).

In the first case (top panel in figure 7*b*), the sensor is moved away from the cylinder, thus measuring information further downstream. This results in the critical zero I moving from the right-half plane (RHP) into the left-half plane (LHP) and the critical zero II moving from the LHP into the RHP. The existence of RHP zeros is problematic for control design because they limit the maximum bandwidth or the maximum frequency that can be controlled with good performance and robustness, as described by Zhou, Doyle & Glover (1996) and Hoagg & Bernstein (2007). In this case, zero I stays in the LHP for $d > 1.6D$ whereas zero II stays in the LHP for $d < 2.4D$. The optimal sensor location at the Reynolds number considered is $d \approx 2.0D$, for which all zeros stay in the LHP (as indicated by ∘ (red) in figure 7). This is also consistent with the fundamental trade-off described above.

Increasing Reynolds number also moves the zeros into the RHP, which can be seen from the root loci plotted beneath. In this case, we fix the sensor location at $d = 2.5D$ and increase Reynolds number from 50 to 110 in intervals of 10. It is interesting to note that increasing Reynolds number not only increases the real part of the unstable pole but also moves these critical zeros towards the RHP. Based on the root loci in the two cases, we can conclude that it becomes harder to find a good sensor location (where no RHP zeros occur) at higher Reynolds numbers. This difficulty leads to a

degradation in the performance and robustness of the optimal controllers at higher Reynolds numbers, as depicted in figure 7(*a*). Furthermore, zero I appears near the unstable pole and moves closer to the unstable pole at higher Reynolds numbers (or more upstream sensor locations), whereas zero II remains at higher frequencies. Due to the bandwidth limitation from the RHP zeros, the optimal control design algorithm would be able to compute a better controller if zero I stays in the LHP. Thus, the systems would prefer a sensor placed further downstream to prevent RHP zero I. This preference is shown by the contour map in figure 7(*a*), where a gentle slope of b_{opt} occurs if the sensor is placed downstream of the optimal location but a rapid drop occurs if the sensor is placed upstream.

Similar maps of system roots are also summarised and analysed in the work of Belson *et al.* (2013), where optimal controllers were designed for a linearised two-dimensional Blasius boundary layer controlled by different types and positions of actuators and sensors. A degradation of the controllers' performance and robustness was observed when RHP zeros occurred. Generally, the physical mechanisms behind the RHP zeros are due to (i) the time delay or (ii) the observability of the structures that are to be controlled. In a flow system, when the sensor is far downstream of the actuator, it measures the effect of the actuator with a time delay due to the convective nature of the flow. That is, the sensor measures flow structures that convected past the actuator at an earlier time. With outdated information, the controller poorly estimates and controls the flow structures near the actuator. This time delay becomes more significant as the sensor moves downstream and results in RHP zeros in the reduced-order transfer function $\widetilde{P}(s)$.

However, with a sensor close to the actuator, the performance and robustness of the optimal controller are still restricted by RHP zeros that occur near the unstable pole. Such RHP zeros cancel the effect of the unstable pole and prevent the sensor from measuring the instability. In other words, the poor performance and robustness of the controller are caused by a lack of observability of the unstable mode instead of excessive time delay.

In this section, we have shown that different sensor locations and Reynolds numbers have similar properties that restrict the performance and robustness of the optimal controllers. At higher Reynolds numbers, even an optimal controller performs poorly for both control set-ups. In other words, the best possible performance that can be achieved is severely restricted. From the perspective of control theory, we observe RHP zeros which limit control performance. Thus, we cannot always find a controller with good performance and robustness, and this can be attributed to the compromise between the observability of the instability and the size of the convective time delay.

5. Body-mounted control set-up case

We now turn our attention to a more physically representative control set-up with a body-mounted actuator and a body-mounted sensor. The schematic diagram is illustrated in figure 1(*b*), where the flow field is now controlled by the oscillation of the cylinder itself, which oscillates in response to the lift measured on the cylinder. Following a procedure similar to that for the in-flow control case, we also consider the physics behind the difficulty in synthesising controllers with good performance and robustness.

5.1. *Open-loop system identification*

The purpose of both control set-ups is to eliminate the perturbations and drive the system towards the steady solution: the base flow. Figure 8 shows the normalised

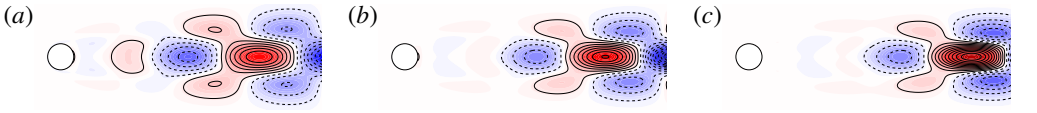

FIGURE 8. Vorticity contours (dashed lines for negative and solid lines for positive vorticity) for the perturbation system (normalised, real part) actuated by the harmonic oscillation of the cylinder at the unstable frequency for (*a*) $Re = 60$, (*b*) $Re = 80$ and (*c*) $Re = 100$. Contour plots share the same scale.

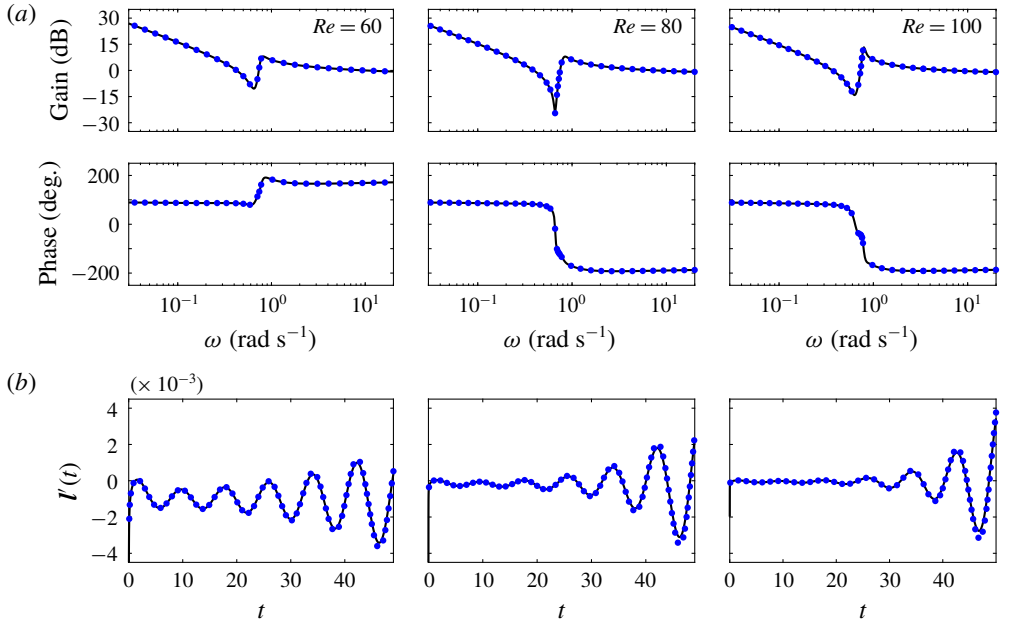

FIGURE 9. (*a*) Frequency responses from $P(j\omega)$ (——) compared to those from ROMs $\widetilde{P}(j\omega)$ (•, blue) at $Re = 60$, 80 and 100. (*b*) The corresponding open-loop impulse responses from numerical simulations. The results for $Re = 60$ and 80 are multiplied by 15 and 3, respectively, so that the same scale can be used.

vorticity field of the corresponding perturbation system $P(s)$ actuated by the oscillation of the cylinder at the instability frequency (i.e. the resolvent operator between the input and output in (3.2)). Similar to the in-flow set-up, the large vortical structure actuated on by the moving cylinder develops further downstream as the Reynolds number increases.

The system identification procedure is carried out in a similar manner to § 4.1 and is summarised in figure 9. The ROMs $\widetilde{P}(s)$ are chosen such that the fitting residual ϵ is below 10^{-5} with orders less than 35. The Bode plots of identified transfer functions between the actuator and the sensor are shown in figure 9(*a*) and compared to the frequency responses of the true systems. Unlike the in-flow set-up, the perturbation system with body-mounted set-up has infinite zero-frequency response (i.e. the system contains an integrator) and constant infinite-frequency response (i.e. the system contains a non-zero feed-forward term).

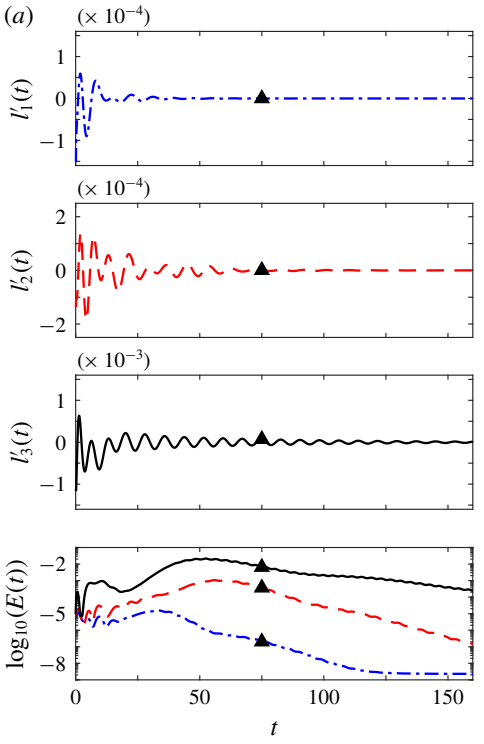

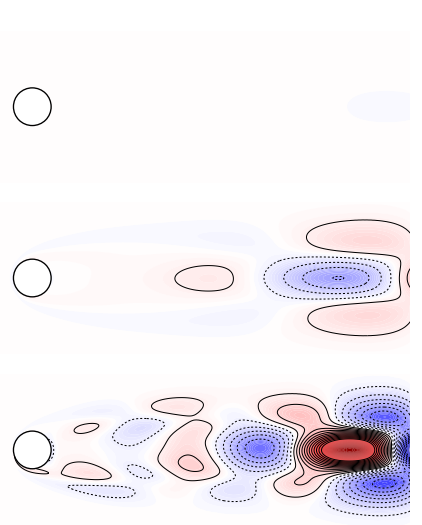

(c)

Re	*k*	*a*	b_{opt}	*d*
60	3.1	0.5	0.2537	–
80	20.0	0.2	0.0764	–
100	0.7	19.8	0.0313	–

FIGURE 10. Direct numerical simulation results of closed-loop systems. (*a*) Time evolution of the cylinder lift and the total perturbation energy $E(t)$ in log scale at $Re = 60$ (– · –, blue), $Re = 80$ (- -, red) and $Re = 100$ (——). (*b*) Vorticity contours (dashed lines for negative and solid lines for positive vorticity) for the perturbation systems at $t = 75$ (▲) at $Re = 60, 80$ and 100 (from top to bottom). All contour plots share the same colour range. (*c*) Table of parameters.

Figure 9(*b*) shows comparisons of open-loop impulse responses (of magnitude 10^{-4}) from the identified models and direct numerical simulations. The excellent agreement observed validates the accuracy of the ROMs.

5.2. *Model-based feedback control*

Following the same procedure as in § 4.2, we design optimal controllers for ROMs and implement them in the full nonlinear Navier–Stokes system actuated by an initial impulse of magnitude 10^{-4}. The parameters of controllers and the corresponding closed-loop simulations are summarised in figure 10. The stabilisation of vortex shedding is achieved only up to $Re = 100$, which can be seen both in the time evolution of the lift $l'(t)$ and in the total perturbation energy $E(t)$. The comparison among simulations at three Reynolds numbers indicates a similar deterioration of control performance to that seen for the in-flow set-up of § 4.

The control of vortex shedding using such body-mounted set-up is more challenging than control with the in-flow set-up in § 4. This is revealed by closed-loop simulations in three ways. First, controllers designed for $Re = 60, 80$ and 100, although stabilising, show poorer performance than controllers designed for the in-flow set-up. Second, the

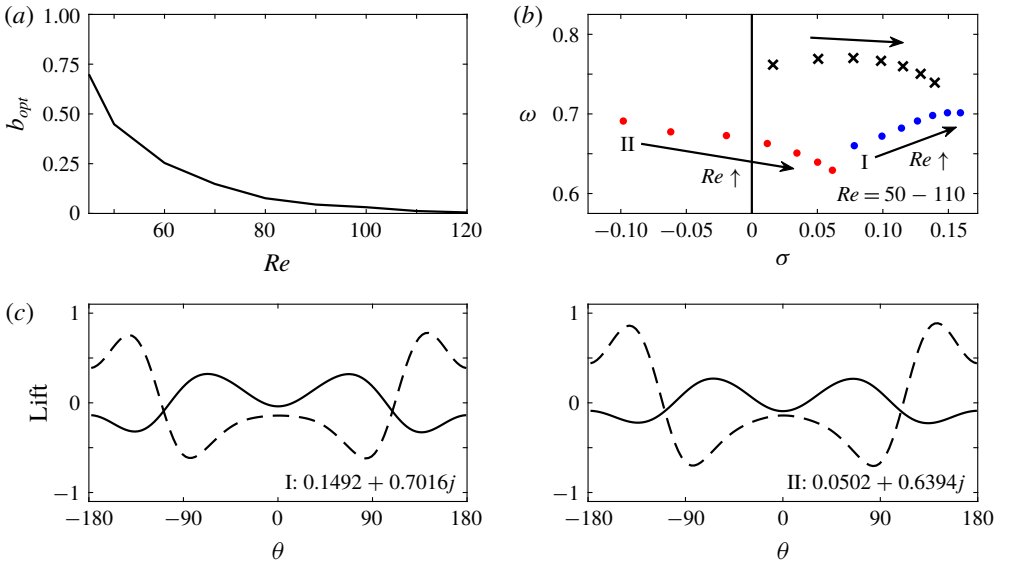

FIGURE 11. (*a*) The largest b_{opt} (——) that can be achieved at different Reynolds numbers. (*b*) Loci of unstable poles (×) and critical zeros (•, blue; •, red) of transfer functions $\widetilde{P}(s)$ at different Reynolds numbers. (*c*) Lift distributions (—— for real part and - - for imaginary part) on the cylinder at RHP zeros I and II and $Re = 100$.

optimal controller fails to stabilise the flow system if the Reynolds number is greater than 100. Third, the optimal stability margin b_{opt}, which is a performance indicator of the controller, decreases from 0.2537 at $Re = 60$ to an extremely small value of 0.0313 at $Re = 100$. This is a much more severe degradation than that seen for the in-flow set-up for which the value decreased from 0.3952 at $Re = 60$ to 0.2495 at $Re = 100$.

A more detailed trend of the optimal stability margin b_{opt} is depicted in figure 11(*a*) as a function of Reynolds number. The severe degradation of control performance is clearly shown by the reduction in b_{opt} from 0.4484 at $Re = 50$ to 0.0313 at $Re = 100$, whereas the optimal stability margin b_{opt} of the in-flow set-up changes from 0.7 to 0.2495 in the same range of Reynolds numbers.

From the perspective of control theory, the performance and robustness of an optimal controller, as quantified by the optimal stability margin b_{opt}, can be affected by the roots (zeros and poles) of the corresponding system, especially those near the unstable mode. In general, each zero blocks a specific input signal and each RHP zero blocks a specific input signal which is unbounded (Hoagg & Bernstein 2007). If a RHP zero occurs at exactly the same location as an unstable pole, it blocks the unstable mode exactly and the instability cannot be measured by the sensor. The system is thus unobservable and no controller is able to stabilise the unstable mode.

Figure 11(*b*) shows the root loci near the unstable mode for the flow systems between $Re = 50$ and $Re = 110$. It can be seen from the figure that as Reynolds number increases, these poles and zeros move into the RHP, which implies stronger instability and more RHP zeros. More importantly, the RHP zero I moves closer to the unstable poles at higher Reynolds numbers, which further blocks the effect of instability and reduces the observability of the unstable mode. This trend can be better observed in table 1, which summarises the stability margin and the distances between

Re	b_{opt}	$\|p_u - z_{\mathrm{I}}\|$	$\|p_u - z_{\mathrm{II}}\|$
50	0.4484	0.1191	—
60	0.2537	0.1086	—
70	0.1481	0.0954	—
80	0.0764	0.0806	0.1354
90	0.0446	0.0657	0.1358
100	0.0313	0.0531	0.1360
110	0.0122	0.0427	0.1350

TABLE 1. Evolution with Reynolds number of stability margin b_{opt} and distance between unstable pole p_u and RHP zero z_i.

the unstable pole and RHP zeros at each Reynolds number. With increasing Reynolds number, the number of RHP zeros is increasing and their distances to the unstable pole are decreasing. The signals from the unstable mode are thus more likely to be blocked by RHP zeros. In other words, the observability of the instability is becoming worse when more RHP zeros move closer to the unstable pole. These RHP zeros are thus problematic for control design and restrict the performance and robustness of optimal controllers. Similar restrictions are also observed from the root loci of the flow system with an in-flow set-up. However, at low Reynolds numbers, the in-flow set-up does not have RHP zeros, whereas in the system with body-mounted set-up, at least one RHP zero occurs near the unstable pole.

For the body-mounted set-up, the sensor and actuator are attached to the cylinder and no time delay should be present in the transfer function from the actuator to the sensor. In other words, none of these RHP zeros is caused by the time delay. To investigate the physical mechanisms represented by these zeros, we take the cylinder flow at $Re = 100$ as an example and plot the lift distributions on the cylinder surface for two RHP zeros in figure 11(*c*). It is interesting to note that even though zero lift should act on the cylinder at these zeros, the force acting on the cylinder surface is non-zero. Instead, the vertical force acting on the rear surface ($-90° < \theta < 90°$) cancels the force acting on the front surface. Such force cancellations always occur near the unstable pole which blocks the signal from the unstable mode and prevents it being measured (the force on the rear surface cancels the force on the front surface). By using an integrated quantity as the measurement, the observability of the unstable mode can either be enhanced or weakened. A previous study tried surface pressure measurements for bluff body control (Dalla Longa, Morgans & Dahan 2017). In that study it was found that doing (pressure on rear top) minus (pressure on rear bottom) gave better performance than summing over the whole surface (i.e. a lift-type measurement).

6. Conclusions

Model-based feedback control of vortex shedding behind a two-dimensional circular cylinder has been investigated. We have built linear ROMs for the linear dynamics of the flow systems about unstable equilibrium states in an input–output framework. The method involves the formulation of the resolvent operator from the linearised flow system to compute frequency responses for control set-ups. We then identify low-order models from these responses using vector fitting methods. The resulting models are capable of accurately capturing the input–output flow behaviour which has been

demonstrated by comparing their impulse responses to direct numerical simulations. Stabilising feedback controllers have been designed for these ROMs based on the $\mathcal{H}_\infty$ loop-shaping procedure of Glover & McFarlane (1989), and validated by applying them to the original high-order nonlinear flow systems. The method has been applied to two single-input single-output control configurations and led to the full stabilisation of the nonlinear flow systems over a range of Reynolds numbers.

To investigate the role of sensor placement in the performance and robustness of the closed loop, we chose an in-flow control set-up with a pair of antisymmetric body forces for actuation and a downstream point sensor measuring the vertical velocity. Different sensor positions have been examined for a range of Reynolds numbers and the corresponding optimal sensor locations indicate two principles of the sensor placement: on the one hand, it should be close enough to the actuator to reduce the time delay due to the highly convective nature of the system; on the other hand, the sensor is required to measure the information developing downstream.

Similar trade-offs have also been observed in the feedback control of the linearised Ginzburg–Landau system by Oehler & Illingworth (2018). Difficulties in satisfying these two conflicting requirements at a higher Reynolds number cause a deterioration in the optimal controller performance and robustness. This deterioration has been shown to be related to the presence of RHP zeros in the transfer function from actuator to sensor as in Belson *et al.* (2013), and the sensor location has been observed to be a significant parameter in feedback flow control. These RHP zeros prevent robust control tools from designing well-behaved controllers and place severe limitations on closed-loop performance.

The method has also been applied to a body-mounted control set-up in which the controller measures the lift on the cylinder and actuates the cylinder's displacement. We controlled the acceleration of the oscillatory cylinder according to its lift measurement and successfully suppressed vortex shedding up to $Re = 100$. The deterioration of the optimal controller's performance and robustness is more severe than for the in-flow sensor set-up at all Reynolds numbers considered. In this control set-up both the sensor and actuator are attached to the cylinder, which implies zero time delay, but the instability developing downstream cannot be sufficiently well captured. This limitation manifests itself in the form of lift cancellations which are represented by RHP zeros near the unstable poles.

This study has presented an efficient modelling approach using the resolvent operator, which does not rely either on expensive direct numerical simulations or on experimental data. It constructs models of sufficient quality to design and implement robust stabilising controllers for unstable flows. In addition, the formulation accounts for actuation and measurements directly, and therefore it can be applied to a broad range of flow control configurations.

Declaration of interests

The authors report no conflict of interest.

REFERENCES

AHUJA, S. & ROWLEY, C. W. 2010 Feedback control of unstable steady states of flow past a flat plate using reduced-order estimators. *J. Fluid Mech.* **645**, 447–478.

ÅKERVIK, E., HŒPFFNER, J., EHRENSTEIN, U. W. E. & HENNINGSON, D. S. 2007 Optimal growth, model reduction and control in a separated boundary-layer flow using global eigenmodes. *J. Fluid Mech.* **579**, 305–314.

AMESTOY, P. R., DUFF, I. S., KOSTER, J. & L'EXCELLENT, J. Y. 2001 A fully asynchronous multifrontal solver using distributed dynamic scheduling. *SIAM J. Matrix Anal. Applics.* **23** (1), 15–41.

AMESTOY, P. R., GUERMOUCHE, A., L'EXCELLENT, J. Y. & PRALET, S. 2006 Hybrid scheduling for the parallel solution of linear systems. *Parallel Comput.* **32** (2), 136–156.

AUBRY, N., HOLMES, P., LUMLEY, J. L. & STONE, E. 1988 The dynamics of coherent structures in the wall region of a turbulent boundary layer. *J. Fluid Mech.* **192**, 115–173.

BAGHERI, S., HENNINGSON, D. S., HOEPFFNER, J. & SCHMID, P. J. 2009 Input-output analysis and control design applied to a linear model of spatially developing flows. *Appl. Mech. Rev.* **62** (2), 020803.

BARKLEY, D. 2006 Linear analysis of the cylinder wake mean flow. *Eur. Phys. Lett.* **75** (5), 750–756.

BELSON, B. A., SEMERARO, O., ROWLEY, C. W. & HENNINGSON, D. S. 2013 Feedback control of instabilities in the two-dimensional blasius boundary layer: the role of sensors and actuators. *Phys. Fluids* **25** (5), 054106.

BRACKSTON, R. D., DE LA CRUZ, J. G., WYNN, A., RIGAS, G. & MORRISON, J. F. 2016 Stochastic modelling and feedback control of bistability in a turbulent bluff body wake. *J. Fluid Mech.* **802**, 726–749.

BRACKSTON, R. D., WYNN, A. & MORRISON, J. F. 2018 Modelling and feedback control of vortex shedding for drag reduction of a turbulent bluff body wake. *Intl J. Heat Fluid Flow* **71**, 127–136.

CHEN, K. K. & ROWLEY, C. W. 2011 $\mathcal{H}_2$ optimal actuator and sensor placement in the linearised complex Ginzburg–Landau system. *J. Fluid Mech.* **681**, 241–260.

CHOI, H., JEON, W. P. & KIM, J. 2008 Control of flow over a bluff body. *Annu. Rev. Fluid Mech.* **40**, 113–139.

DAHAN, J. A., MORGANS, A. S. & LARDEAU, S. 2012 Feedback control for form-drag reduction on a bluff body with a blunt trailing edge. *J. Fluid Mech.* **704**, 360–387.

DALLA LONGA, L., MORGANS, A. S. & DAHAN, J. A. 2017 Reducing the pressure drag of a D-shaped bluff body using linear feedback control. *Theor. Comput. Fluid Dyn.* **31** (5-6), 567–577.

DESCHRIJVER, D., MROZOWSKI, M., DHAENE, T. & DE ZUTTER, D. 2008 Macromodeling of multiport systems using a fast implementation of the vector fitting method. *IEEE Microw. Wirel. Compon. Lett.* **18** (6), 383–385.

DUŠEK, J., LE GAL, P. & FRAUNIÉ, P. 1994 A numerical and theoretical study of the first Hopf bifurcation in a cylinder wake. *J. Fluid Mech.* **264**, 59–80.

FLINOIS, T. L. & MORGANS, A. S. 2016 Feedback control of unstable flows: a direct modelling approach using the eigensystem realisation algorithm. *J. Fluid Mech.* **793**, 41–78.

GIANNETTI, F. & LUCHINI, P. 2007 Structural sensitivity of the first instability of the cylinder wake. *J. Fluid Mech.* **581**, 167–197.

GILLIES, E. A. 1998 Low-dimensional control of the circular cylinder wake. *J. Fluid Mech.* **371**, 157–178.

GLOVER, K. & MCFARLANE, D. 1989 Robust stabilization of normalized coprime factor plant descriptions with h_∞-bounded uncertainty. *IEEE Trans. Autom. Control* **34** (8), 821–830.

GÓMEZ, F., BLACKBURN, H. M., RUDMAN, M., SHARMA, A. S. & MCKEON, B. J. 2016 A reduced-order model of three-dimensional unsteady flow in a cavity based on the resolvent operator. *J. Fluid Mech.* **798**, R2.

GUNZBURGER, M. D. & LEE, H. C. 1996 Feedback control of Karman vortex shedding. *Trans. ASME J. Appl. Mech.* **63** (3), 828–835.

GUSTAVSEN, B. 2006 Improving the pole relocating properties of vector fitting. *IEEE Trans. Power Deliv.* **21** (3), 1587–1592.

GUSTAVSEN, B. 2013 The vector fitting website, *MATLAB code*, 21. Available at: https://www.sintef.no/projectweb/vectorfitting/.

GUSTAVSEN, B. & SEMLYEN, A. 1999 Rational approximation of frequency domain responses by vector fitting. *IEEE Trans. Power Deliv.* **14** (3), 1052–1061.

HOAGG, J. B. & BERNSTEIN, D. S. 2007 Nonminimum-phase zeros – much to do about nothing – classical control – revisited part II. *IEEE Control Syst. Mag.* **27** (3), 45–57.

ILAK, M. & ROWLEY, C. W. 2008 Modeling of transitional channel flow using balanced proper orthogonal decomposition. *Phys. Fluids* **20** (3), 034103.

ILLINGWORTH, S. J. 2016 Model-based control of vortex shedding at low Reynolds numbers. *Theor. Comput. Fluid Dyn.* **30** (5), 429–448.

JACKSON, C. P. 1987 A finite-element study of the onset of vortex shedding in flow past variously shaped bodies. *J. Fluid Mech.* **182**, 23–45.

JUANG, J. N. & PAPPA, R. S. 1985 An eigensystem realization algorithm for modal parameter identification and model reduction. *J. Guid. Control Dyn.* **8** (5), 620–627.

KIM, J. & BEWLEY, T. R. 2007 A linear systems approach to flow control. *Annu. Rev. Fluid Mech.* **39**, 383–417.

LEONTINI, J. S., STEWART, B. E., THOMPSON, M. C. & HOURIGAN, K. 2006 Wake state and energy transitions of an oscillating cylinder at low Reynolds number. *Phys. Fluids* **18** (6), 067101.

LOGG, A., MARDAL, K. A. & WELLS, G. 2012 *Automated Solution of Differential Equations by the Finite Element Method: The FEniCS Book*, vol. 84. Springer Science & Business Media.

MA, Z., AHUJA, S. & ROWLEY, C. W. 2011 Reduced-order models for control of fluids using the eigensystem realization algorithm. *Theor. Comput. Fluid Dyn.* **25** (1-4), 233–247.

MCKEON, B. J. & SHARMA, A. S. 2010 A critical-layer framework for turbulent pipe flow. *J. Fluid Mech.* **658**, 336–382.

MORTENSEN, M., LANGTANGEN, H. P. & WELLS, G. N. 2011 A fenics-based programming framework for modeling turbulent flow by the Reynolds-averaged Navier–Stokes equations. *Adv. Water Resour.* **34** (9), 1082–1101.

MUDDADA, S. & PATNAIK, B. S. V. 2010 An active flow control strategy for the suppression of vortex structures behind a circular cylinder. *Eur. J. Mech. (*B*/Fluids)* **29** (2), 93–104.

NGUYEN, V. D., JANSSON, J., GOUDE, A. & HOFFMAN, J. 2019 Direct finite element simulation of the turbulent flow past a vertical axis wind turbine. *Renew. Energy* **135**, 238–247.

OEHLER, S. F. & ILLINGWORTH, S. J. 2018 Sensor and actuator placement trade-offs for a linear model of spatially developing flows. *J. Fluid Mech.* **854**, 34–55.

PARK, D. S., LADD, D. M. & HENDRICKS, E. W. 1994 Feedback control of von Kármán vortex shedding behind a circular cylinder at low Reynolds numbers. *Phys. Fluids* **6** (7), 2390–2405.

PIER, B. 2002 On the frequency selection of finite-amplitude vortex shedding in the cylinder wake. *J. Fluid Mech.* **458**, 407–417.

PROVANSAL, M., MATHIS, C. & BOYER, L. 1987 Bénard–von Kármán instability: transient and forced regimes. *J. Fluid Mech.* **182**, 1–22.

ROUSSOPOULOS, K. 1993 Feedback control of vortex shedding at low Reynolds numbers. *J. Fluid Mech.* **248**, 267–296.

ROWLEY, C. W. 2005 Model reduction for fluids, using balanced proper orthogonal decomposition. *Intl J. Bifurcation Chaos* **15** (03), 997–1013.

ROWLEY, C. W. & DAWSON, S. T. 2017 Model reduction for flow analysis and control. *Annu. Rev. Fluid Mech.* **49**, 387–417.

SINGH, S. N., MYATT, J. H., ADDINGTON, G. A., BANDA, S. & HALL, J. K. 2001 Optimal feedback control of vortex shedding using proper orthogonal decomposition models. *Trans. ASME J. Fluids Engng* **123** (3), 612–618.

SIPP, D. & MARQUET, O. 2013 Characterization of noise amplifiers with global singular modes: the case of the leading-edge flat-plate boundary layer. *Theor. Comput. Fluid Dyn.* **27** (5), 617–635.

SIPP, D., MARQUET, O., MELIGA, P. & BARBAGALLO, A. 2010 Dynamics and control of global instabilities in open-flows: a linearized approach. *Appl. Mech. Rev.* **63** (3), 030801.

SON, D. & CHOI, H. 2018 Iterative feedback tuning of the proportional-integral-differential control of flow over a circular cylinder. *IEEE Trans. Control Syst. Technol.* **27** (4), 1385–1396.

SON, D., JEON, S. & CHOI, H. 2011 A proportional–integral–differential control of flow over a circular cylinder. *Phil. Trans. R. Soc. Lond.* A **369** (1940), 1540–1555.

SYMON, S., ROSENBERG, K., DAWSON, S. T. & MCKEON, B. J. 2018 Non-normality and classification of amplification mechanisms in stability and resolvent analysis. *Phys. Rev. Fluids* **3** (5), 053902.

TAIRA, K., BRUNTON, S. L., DAWSON, S. T., ROWLEY, C. W., COLONIUS, T., MCKEON, B. J., SCHMIDT, O. T., GORDEYEV, S., THEOFILIS, V. & UKEILEY, L. S. 2017 Modal analysis of fluid flows: an overview. *AIAA J.* **55** (12), 4013–4041.

VASILYEVA, M., CHUNG, E. T., EFENDIEV, Y. & KIM, J. 2019 Constrained energy minimization based upscaling for coupled flow and mechanics. *J. Comput. Phys.* **376**, 660–674.

WILLIAMSON, C. H. K. 1996 Vortex dynamics in the cylinder wake. *Annu. Rev. Fluid Mech.* **28** (1), 477–539.

YAO, W. & JAIMAN, R. K. 2017*a* Feedback control of unstable flow and vortex-induced vibration using the eigensystem realization algorithm. *J. Fluid Mech.* **827**, 394–414.

YAO, W. & JAIMAN, R. K. 2017*b* Model reduction and mechanism for the vortex-induced vibrations of bluff bodies. *J. Fluid Mech.* **827**, 357–393.

ZEBIB, A. 1987 Stability of viscous flow past a circular cylinder. *J. Engng Maths* **21** (2), 155–165.

ZHANG, M. M., CHENG, L. & ZHOU, Y. 2004 Closed-loop-controlled vortex shedding and vibration of a flexibly supported square cylinder under different schemes. *Phys. Fluids* **16** (5), 1439–1448.

ZHOU, K., DOYLE, J. C. & GLOVER, K. 1996 *Robust and Optimal Control*, vol. 40. Prentice Hall.